River Flow 2016 – Constantinescu, Garcia & Hanes (Eds)
© 2016 Taylor & Francis Group, London, ISBN 978-1-138-02913-2

Photometric velocity tracking tool for laboratory generated turbidity currents

R.I. Wilson & H. Friedrich
University of Auckland, Auckland, New Zealand

C. Stevens
National Institute of Water and Atmospheric Research, Wellington, New Zealand

ABSTRACT: We present a photometric method for velocity measurement and filtering of turbidity current noses interacting with obstacles. Photometry is an emerging experimental technique for laboratory turbidity currents due to its non-intrusive nature on flow. Costs to employ the technique are ever-reducing as technology advances. Experimental turbidity currents of varying density interacting with an obstacle are captured at 120 fps. Images are filtered through a range of algorithms to reduce noise induced from the presence of UVP and siphon mounting racks. The location of the current nose is successfully tracked over time, allowing insight into the development of current velocities at the leading boundary. Velocities of tests with no obstacle were found to be consistent over time, showing the current to be within the buoyancy-dominant phase. Velocities including an obstacle varied significantly due to current interaction. This non-intrusive measurement and filtering technique provides a new approach to obtaining qualitative information of opaque turbidity currents, particularly the study of currents interacting with obstacles, where conventional measurement techniques are physically difficult to implement due to their intrusive nature.

1 INTRODUCTION

Sediment-laden flows, or turbidity currents, are a type of buoyancy driven flow. Such flows are initiated when gravity acts upon the relatively small density difference of the sediment-entrained fluid and an ambient fluid (Middleton, 1993). They are known to be major agents of sediment transport in oceans, seas, lakes and on land (Kneller and Buckee, 2000). Such currents are generally initiated from natural events such as earthquakes mobilizing submarine sediment, or rivers in flood depositing sediment onto the ocean floor (Meiburg and Kneller, 2010). They can also be formed from anthropogenic activities such as dredging, or bottom trawling operations causing sediment resuspension (Pilskaln et al., 1998).

There has been increased interest in turbidity current research over the past three decades, particularly their flow characteristics. This interest has partially been driven by the detrimental effects turbidity currents can have on engineered structures. Turbidity currents have been attributed to causing submarine cable damage (Heezen and Ewing, 1952, Hsu et al., 2008). This risk is likely to only increase, given there has been an exponential increase in internet communications, of which over 95% occur via the use of submarine cables (Carter et al., 2009). Similarly, turbidity currents are an environmental and economic threat to oil pipelines and structures. For example, the proposed Middle East India Deepwater Pipeline (MEIDP) is planned to cross five submarine canyons, where turbidity currents have been outlined as one of the key hazards to operations (Nash et al., 2014).

In recent years, there has been an increase in experimental and computational studies of saline gravity currents interacting with obstacles, stemmed by a need to understand their flow characteristics so their effect on submarine structures can be predicted or mitigated. However to the authors' knowledge there are far fewer studies on obstacles applying sediment-laden flows (Alexander and Morris, 1994, Morris and Alexander, 2003, Oehy and Schleiss, 2007, Stevenson and Peakall, 2010, Oshaghi et al., 2013, McArthur et al., 2014, Wilson and Friedrich, 2014, Wilson, 2015, Wilson et al., 2015). The use of sediment-entrained currents in laboratory experiments provides a more representative model of turbidity currents than saline flows, by recreating important processes such as deposition and entrainment of sediment.

Quantitative data of experimental turbidity currents is generally obtained through conventional

flow measurement techniques such as ADV, UDVP and density sampling. More recent techniques such as photometry have seldom been adopted. Photometry is becoming a popular laboratory technique for tracking the development of saline current profiles and holds great promise for sediment-laden flows. This is both due to increases in available technology and the relatively cheap cost of instrumentation compared to measurements with UVP or ADV probes. It allows visual insight into current properties, such as Kelvin-Helmholtz instabilities and lobe/cleft structures that occur at the density interfaces. Previous studies have also obtained space-time location of current heads using image thresholding techniques (Adduce et al., 2012, Jacobson and Testik, 2014, Lombardi et al., 2015, Mirajkar et al., 2015, Nogueira et al., 2013a, Nogueira et al., 2013b, Nogueira et al., 2014). Image thresholding techniques involve converting captured images of currents to greyscale format and comparing each individual pixel's light intensity against a chosen threshold. Most commonly, the back wall of the flume is illuminated with strip fluorescents, which creates a bright background and dark silhouette of the current when it passes the analysis area. The threshold is generally determined by assessing the intensity of pixels within the boundary of the current. Therefore pixels above and below this threshold are converted to opposite binary values, which creates a binary outline of the current. This technique is attractive for turbidity currents interacting with obstacles because of its non-intrusive nature on flow, and ability to capture boundary information in detail near obstacles, which would otherwise be physically difficult and intrusive with conventional flow measurement techniques. However, the inclusion of obstacles and instrument racks within the flume cause visual obstruction of the current boundary which can result in incorrect boundary recognition when using the thresholding technique.

The following study therefore presents a novel adaptation of the image thresholding technique for obtaining horizontal velocities of turbidity currents interacting with obstacles. Plan and front-facing lighting is used to illuminate the current against a dark background instrument. Experimental turbidity currents are analyzed both with and without an obstacle. Various velocity filtering techniques are applied to eliminate noise and provide quantitative values of turbidity current nose velocity.

2 METHODOLOGY

2.1 *Experimental setup*

Turbidity currents composed of 1:1 ratio of kaolinite and spherical glass beads were released in an acrylic lock-exchange flume within the Hydraulic Engineering Laboratory at the University of Auckland (Fig. 1). The 400 mm wide, and 5 m long flume, had 0.8 mm sand glued to the bed to create a rough bed surface. A 140 mm × 50 mm rectangular obstacle was placed across the width of the flume at a location of 3700 mm from the lock gate.

A Lumenera LT425 CMOS camera was located adjacent to the flume wall at a location of approximately ¾ towards the downstream end of the flume. The camera recorded raw images at a resolution of 2048 × 1504 pixels and a framerate of 120 fps. To the knowledge of the author, such a high framerate has not been applied in the analysis of turbidity currents. A Nikon 50 mm f/1.8 lens was attached to the camera and focused on an allocated analysis area within the flume. The camera recorded the complete passing of the generated turbidity current through the field of view. The flume was front-lit using two halogen lamps in elevation view and two in plan view. Such lighting was chosen as an alternative to common back-lighting due to the inclusion of the obstacle, UVP and siphon racks which would create a greater visual impairment of current boundaries to a back-lit current. A series of calibration tests were carried out to optimize the lighting conditions and ensure the turbidity current showed a high visual contrast to the back wall. This process is documented in a previous study (Wilson, 2015).

Four different current densities were tested; ρ = 1020, 1040, 1060 and 1080 kgm^{-3}. Each of these densities were tested and repeated without the obstacle present, thus a total of 8 tests were completed. For each test, the flume was filled with tap water to a height of 300 mm at the gate. The calculated sediment mass and 6 L of water was mechanically mixed in a bucket. An equal displacement volume was removed from the lock-box and the slurry was poured in. This displacement volume was used to minimize the head difference between the lock-box and flume, which prior tests showed a difference caused unwanted surface waves. The lock-box gate was then fully opened and the camera set to record until the current had passed the analysis area.

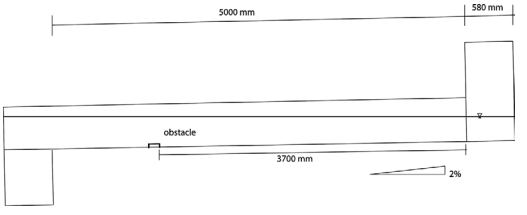

Figure 1. Flume dimensions and obstacle location.

2.2 *Image analysis*

Raw images obtained from the camera were batch processed in Photoshop for correction of lens distortion. All images were then imported into MATLAB, where a series of image manipulation and filtering processes were applied. Images were firstly rotated to account for the 2% slope of the flume. A mm-pixel ratio was then found for each test by measuring the pixel length of the horizontal and vertical calibration rulers. This allowed spatial dimensions to be applied to the turbidity currents. Next, all images were cropped to the final analysis area and converted to greyscale. Intensity levels of each pixel were than compared with an allocated threshold level. Pixels with a light intensity higher than the threshold level were considered to be within the turbidity current, whilst those with a lower light intensity were deemed to be within the ambient background. Opposite bit values were assigned to each condition, creating a binary image of the delineated current. The threshold level for each test was optimized by visually assessing the accuracy of the boundary recognition.

Care was taken to ensure that the flume bed, background and instrument racks had low levels of light intensity, thus were painted black. However, complete light isolation was not possible due to unavoidable bubbles which would sometimes emit from siphon tubes when the current passed the obstacle. These bubbles would cause areas of high light intensity, thus be recognized as part of the turbidity current. Therefore an algorithm was developed which traced all binary confines and identified the longest path as the leading boundary of the turbidity current. All smaller paths were disregarded as noise. An example of a delineated current is shown in Figure 2.

For each image, the forward-most pixel identified as part of the turbidity current was deemed the leading front of the current head. The coordinates and time were recorded for this point, which is shown as the red 'x' in Figure 2.

All images for each test were subsequently processed with the above steps, giving a temporal evolution of the current boundary and outlining the path of the current nose (Fig. 3). This provided a detailed visualization of the current structures and their spatial development over time.

Horizontal velocities of the current nose were calculated from the spatial and temporal evolution between each image. Because of irregularities in current delineation, noise was present in the velocities. Therefore velocities, U_n, which were outside a 100-point rolling standard deviation width of 1σ (Equation 1), were replaced with the mean of the 50 preceding and proceeding velocities. This is a similar method to Keevil et al. (2006).

$$\sigma_n = \sqrt{\frac{1}{2N+1}\left[\sum_{i=1}^{N}\left[(U_{n-i}-\mu)^2+(U_{n+i}-\mu)^2\right]+(U_n-\mu)^2\right]} \quad (1)$$

Where

$$\mu = \frac{1}{2N+1}\left[\sum_{i=1}^{N} U_{n-i} + U_{n+i} + U_n\right] \quad (2)$$

And $N = 50$.

Each end of the velocity data set was concatenated with matrix of length N, which held the average of the first and last 5 velocity values, respectively. It was found that the above filtering process ignored some known errors based off

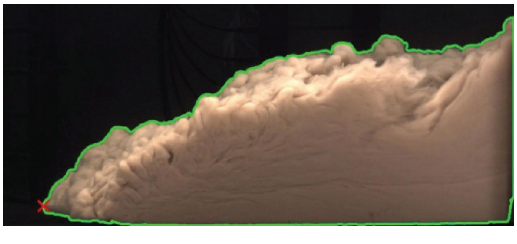

Figure 2. Example of turbidity current boundary recognition.

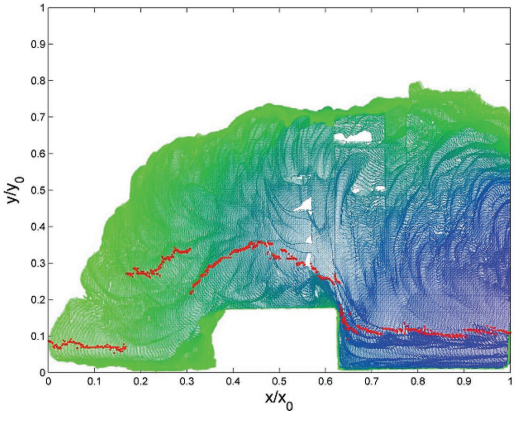

Figure 3. Spatial contour plot detailing the temporal evolution of a turbidity current traversing over a rectangular obstacle. Delineated boundaries for all images of a test were plotted at their time frequency of 120 Hz. Each boundary was given a color between blue and green, as a fraction of the total time to traverse the analysis area. The position of the current nose in each image is tracked, shown in red.

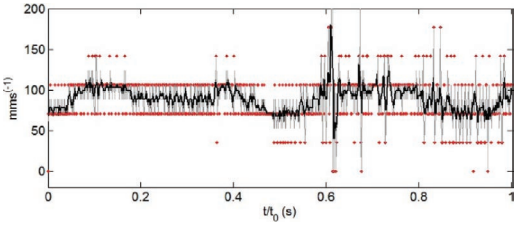

Figure 4. Horizontal velocity plot of a current nose, detailing the filtering process. Red points: raw velocity; gray line: applied standard deviation filter; black line: the final, padded velocity.

review of the boundary delineation, therefore prior to applying the standard deviation filter these data sections were removed and replaced with interpolated values. This was only applied to 3 sections of O1080.1.

Once noise peaks were removed, a 20-point moving mean was applied to the velocity data in order to calculate sub-pixel velocity values. Figure 4 gives an example of the raw and filtered velocity data. The filters were applied to all eight tests, allowing nose velocities to be compared.

3 RESULTS AND DISCUSSIONS

Figures 5 and 6 show velocity time series of the eight tests. Non-dimensionalization of velocities was not applied, as the key objective of this study was to develop a velocity tracking technique and filtering process for turbidity currents interacting with obstacles. Therefore velocity scaling was ignored. Velocity measurements in future tests are intended to be scaled accordingly so that characteristics may be compared with field studies.

Figure 5 shows velocity data from tests without the obstacle, whilst Figure 6 shows tests with the obstacle. Time was non-dimensionalized as the fraction of the time taken for the current head in test $\rho = 1020$ kgm^{-3} to travel the width of the analysis area.

It is evident that the filtered data provides sub-pixel velocity values. Raw velocities appear to be grouped into set values, which is likely due to the high framerate. This results in a small pixel distance between the front position in each image, thus errors in delineation will have a higher ratio than if a lower capture frequency was used. A solution may be to use a larger time and space step on each image, however the decrease in sensitivity will need to be considered. As expected, there is a clear relationship between current density and velocity for both obstacle scenarios. Average velocity increases with density due to the increase in the

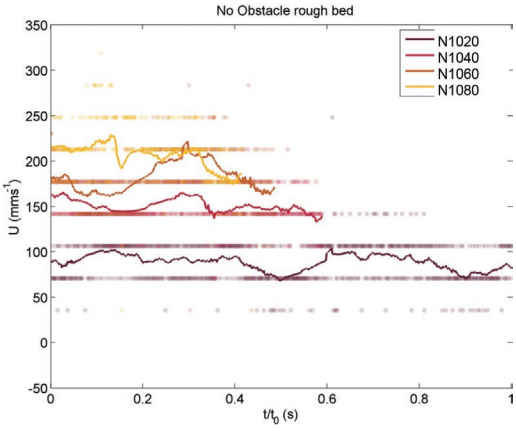

Figure 5. Current front velocity time series for no obstacle tests, detailing the filtering process. Raw data are shown as points and filtered data as lines.

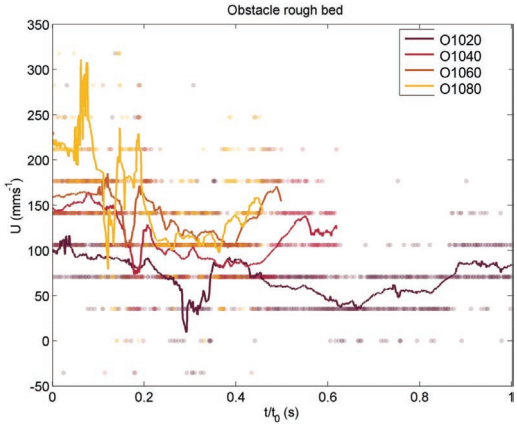

Figure 6. Current front velocity time series for tests involving the obstacle, detailing the filtering process. Raw data are shown as points and filtered data as lines.

driving buoyancy force of the current head. It can be seen for the no-obstacle tests that there are local fluctuations of ~±50 mms^{-1} which may be due to reflected ambient waves off the back of the flume. However, over the time window the velocities of each test appear to have no or minimal decrease in velocity. This confirms that the current is still within the initial slumping phase, where buoyancy forces dominate viscous and inertial forces. Rottman and Simpson (1983) showed that velocity remains constant within this phase. The location of the analysis area is also within the expected length of the slumping phase, which Rottman and Simpson (1983) showed to span approximately 5–10 times the lock-box length.

For the obstacle tests, all velocity time series show an abrupt drop in velocity when the current collides with the front face of the obstacle and propagates upwards.

This is followed by a sharp increase when the current continues forward over the top of the obstacle. There is then a slow decrease as the current head continues to expand upwards. Finally there is a gradual increase in velocity as the nose falls over the downstream end of the obstacle and begins to form a new head. During this phase the vertical rate of expansion also visually appears to decrease. This shows potential for finding quantitative ratios between the observed velocity fluctuations and other variables such as current expansion height, density, and substrate roughness.

Figures 7 and 8 show the spatial path (right to left) of the current nose for the different obstacle configurations and densities. X and Y length scales are non-dimensionalized over the extents of the analysis area. Figure 7 shows there is little variability ($y/y_0 \approx 0.1$) of current nose height for the tests without an obstacle, which is expected. There does however appear to be a small decrease in height for all tests. Noise is apparent at $x/x_0 \approx 1$ for N1020, which is likely due to the point source nature of the halogen lighting and vertical calibration ruler causing a small shadowed area, hence inconsistent delineation. Likewise there appears to be noise at $x/x_0 \approx 0.4$ and $x/x_0 \approx 6$, where the imprint of the obstacle on the front wall has caused light areas to be incorrectly recognized as part of the current. Sensitivity analysis showed these noise effects to be much more prominent if the developed current-detection-by-longest-perimeter algorithm was not applied.

In contrast, Figure 8 shows a large variability of $y/y_0 \approx 0.5$ in current nose height. All tests

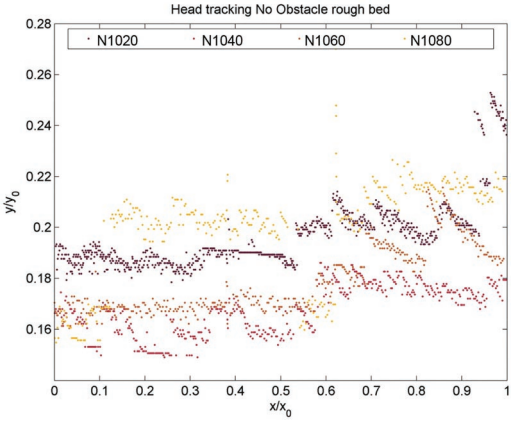

Figure 7. Current front position time series for no obstacle tests.

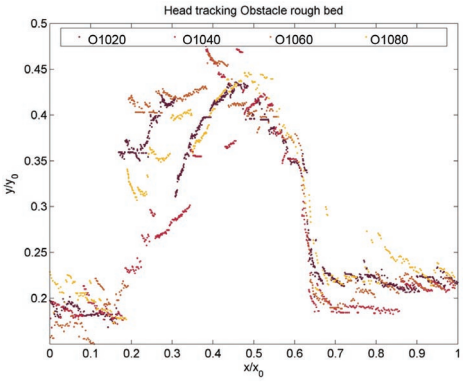

Figure 8. Current front position time series for no obstacle tests.

show a relatively constant nose height until collision with the obstacle takes place, where there is a large upwards trend. As the nose resumes forward movement over the remainder of the obstacle, the height of the leading edge appears to jump. This is likely due to the continual upwards expansion of the nose head which creates a 'blunt' current head with competing frontal lobes. This variability appears to cease when the current head starts to reform after the obstacle at $x/x_0 \approx 0.2$.

Overall, the applied velocity measurement technique for sediment-laden currents interacting with obstacles is shown to be useful for observing flow characteristics, and provides a promising start for future investigations. The filters used are shown to improve the quality of captured photometric data and allow photometry to be successfully combined with conventional, intrusive flow measurement techniques. This is particularly useful when the photometric technique is combined with density siphons, as flow density of opaque, sediment-laden currents is difficult to obtain through photometric processes.

4 CONCLUSIONS AND FUTURE OUTLOOK

The use of photometry to generate quantitative velocity data of opaque turbidity currents interacting with obstacles and surrounded by submerged instrument racks is shown to be feasible. Additionally, the standard deviation and moving average filtering techniques developed are able to significantly improve the quality and usefulness of velocity data. The measurement methodology provides a novel, workable method for combining photometry and intrusive measurement techniques such as density siphoning, UVP and ADV. However, further

investigation into appropriate lengths time-space windows for velocity calculation is warranted.

Velocity time series of the current nose showed a positive relationship between current density and nose velocity. When no obstacle was present in the flume, these velocities were relatively constant, whilst presence of an obstacle caused an abrupt drop in velocity upon interaction, followed by a gradual decrease and increase in velocity as the current head continued to expand upwards and reform after the obstacle.

Velocity tracking of the current nose as it interacts with the obstacle provides an alternative starting point for further velocity-based analyses such as spectral analysis and Froude number/Reynold number parameterization. It is planned to use this novel technique to new insights into how nose velocities are affected by varying obstacle shape and bed roughness.

REFERENCES

Adduce, C., Sciortino, G. & Proietti, S. 2012. Gravity Currents Produced by Lock Exchanges: Experiments and Simulations with a Two-Layer Shallow-Water Model with Entrainment. *Journal of Hydraulic Engineering,* 138, 111–121.

Alexander, J. & Morris, S. 1994. Observations on experimental, nonchannelized, high-concentration turbidity currents and variations in deposits around obstacles. *Journal of Sedimentary Research,* 64, 899–909.

Carter, L., Programme, U.N.E. & Centre, W.C.M. 2009. *Submarine Cables and the Oceans: Connecting the World*, UNEP World Conservation Monitoring System.

Heezen, B.C. & Ewing, M. 1952. Turbidity currents and submarine slumps, and 1929 grand banks earthquake. *American Journal of Science*, 250, 849–873.

Hsu, S.K., Kuo, J., Lo, C.L., Tsai, C.H., Doo, W.B., Ku, C.Y. & Sibuet, J.C. 2008. Turbidity currents, submarine landslides and the 2006 Pingtung earthquake off SW Taiwan. *Terrestrial, Atmospheric and Oceanic Sciences*, 19, 767–772.

Jacobson, M.R. & Testik, F.Y. 2014. Turbulent entrainment into fluid mud gravity currents. *Environmental Fluid Mechanics*, 14, 541–563.

Keevil, G.M., Peakall, J., Best, J.L. & Amos, K.J. 2006. Flow structure in sinuous submarine channels: Velocity and turbulence structure of an experimental submarine channel. *Marine Geology*, 229, 241–257.

Kneller, B. & Buckee, C. 2000. The structure and fluid mechanics of turbidity currents: a review of some recent studies and their geological implications. *Sedimentology*, 47, 62–94.

Lombardi, V., Adduce, C., Sciortino, G. & La Rocca, M. 2015. Gravity currents flowing upslope: Laboratory experiments and shallow-water simulations. *Physics of Fluids*, 27, 016602.

Mcarthur, J.M., Wilson, R.I. & Friedrich, H. 2014. Photometric analysis of the effect of substrates and obstacles on unconfined turbidity current flow propagation. *Reservoir Sedimentation—Special Session on Reservoir Sedimentation of the 7th International Conference on Fluvial Hydraulics, RIVER FLOW 2014*.

Meiburg, E. & Kneller, B. 2010. Turbidity Currents and Their Deposits. *Annual Review of Fluid Mechanics*, 42, 135–156.

Middleton, G.V. 1993. Sediment Deposition from Turbidity Currents. *Annual Review of Earth and Planetary Sciences*, 21, 89–114.

Mirajkar, H.N., Tirodkar, S. & Balasubramanian, S. 2015. Experimental study on growth and spread of dispersed particle-laden plume in a linearly stratified environment. *Environmental Fluid Mechanics*.

Morris, S.A. & Alexander, J. 2003. Changes in Flow Direction at a Point Caused by Obstacles During Passage of a Density Current. *Journal of Sedimentary Research,* 73, 621–629.

Nash, I., Burnett, C. & Smith, R. 2014. Middle East India Deepwater Pipeline (MEIDP) crossing of the Indus Fan. Offshore Technology Conference.

Nogueira, H.I.S., Adduce, C., Alves, E. & Franca, M. 2013a. Image analysis technique applied to lock-exchange gravity currents. *Measurement Science and Technology*, 24, 047001.

Nogueira, H.I.S., Adduce, C., Alves, E. & Franca, M.J. 2013b. Analysis of lock-exchange gravity currents over smooth and rough beds. *Journal of Hydraulic Research*, 51, 417–431.

Nogueira, H.S., Adduce, C., Alves, E. & Franca, M. 2014. Dynamics of the head of gravity currents. *Environmental Fluid Mechanics*, 14, 519–540.

Oehy, C. & Schleiss, A. 2007. Control of Turbidity Currents in Reservoirs by Solid and Permeable Obstacles. *Journal of Hydraulic Engineering*, 133, 637–648.

Oshaghi, M.R., Afshin, H. & Firoozabadi, B. 2013. Experimental investigation of the effect of obstacles on the behavior of turbidity currents. *Canadian Journal of Civil Engineering*, 40, 343–352.

Pilskaln, C.H., Churchill, J.H. & Mayer, L.M. 1998. Resuspension of Sediment by Bottom Trawling in the Gulf of Maine and Potential Geochemical Consequences. *Conservation Biology*, 12, 1223–1229.

Rottman, J.W. & Simpson, J.E. 1983. Gravity currents produced by instantaneous releases of a heavy fluid in a rectangular channel. *Journal of Fluid Mechanics*, 135, 95–110.

Stevenson, C.J. & Peakall, J. 2010. Effects of topography on lofting gravity flows: Implications for the deposition of deep-water massive sands. *Marine and Petroleum Geology*, 27, 1366–1378.

Wilson, R.I. 2015. Optimisation of lighting techniques for photometric measurement of sediment-laden flows. *36th International IAHR World Congress*. Delft—The Hague, the Netherlands.

Wilson, R.I. & Friedrich, H. 2014. Dynamic analysis of the interaction between unconfined turbidity currents and obstacles. *9th International Symposium on Ultrasonic Doppler Methods for Fluid Mechanics and Fluid Engineering*. Strasbourg, France.

Wilson, R.I., Friedrich, H. & Stevens, C. 2015. Intrusive measurement evaluation for sediment-laden flows interacting with an obstacle. *36th International IAHR World Congress*. Delft—The Hague, the Netherlands.